JOURNAL OF AIRCRAFT
Vol. 42, No. 4, July–August 2005

Airbus, ONERA, and DLR Results from the Second AIAA Drag Prediction Workshop

Olaf Brodersen* and Mark Rakowitz*
DLR, German Aerospace Center, 38108 Braunschweig, Germany
Stephane Amant† and Pascal Larrieu†
Airbus France, 31060 Toulouse, France
Daniel Destarac‡
ONERA, 92322 Châtillon, France
and
Mark Sutcliffe‡
Airbus Deutschland, 28183 Bremen, Germany

The results from DLR, German Aerospace Center, Airbus, and ONERA from the Second AIAA CFD Drag Prediction Workshop are presented. The lift, drag, and pitching moments are calculated for the DLR-F6 configuration at transonic flow conditions by solving the Reynolds-averaged Navier–Stokes equations on structured as well as on unstructured, hybrid grids. First, the drag is computed with the standard near-field method by integrating the surface pressure forces and shear stresses and second by a drag breakdown into its physical components, such as viscous, wave, and induced drag, by applying a far-field method. The influence of the grid is investigated, and the results are compared to experimental data. For all cases a slightly smaller angle of incidence is required in the computations as compared to the experiments to obtain the same lift coefficient. The drag polars and the engine installation drag can be computed accurately, but significant deviations exist for the pitching moments as a result of an underestimation of the flow separation at the trailing edge of the upper wing upper. Comparing the far-field drag breakdown results for structured and unstructured solution methods shows that viscous and wave drag are computed nearly identical. The far-field method gives a better understanding of the sources of drag and offers a substantial benefit for aerodynamic design.

Nomenclature

C_D	=	total drag coefficient
C_L	=	total lift coefficient
c	=	local chord length
D_f	=	friction drag
D_i	=	induced drag
D_p	=	pressure drag
D_v	=	viscous drag
D_w	=	wave drag
H	=	stagnation enthalpy
M	=	Mach number
$\boldsymbol{n}$	=	normal vector
p	=	pressure
$\boldsymbol{q}$	=	velocity vector
R	=	gas constant
Re	=	Reynolds number
S	=	surface
s	=	entropy
u	=	velocity component in freestream direction
V_V	=	volume for viscous drag
V_W	=	volume for wave drag
x_{TE}, z_{TE}	=	horizontal, vertical distance of the nacelle from the wing
α	=	angle of incidence
γ	=	ratio of specific heats
ρ	=	density
τ	=	shear stress

Subscripts

A	=	aircraft
f	=	friction
i	=	induced
p	=	pressure
TE	=	trailing edge
v, V	=	viscous
w, W	=	wave
∞	=	freestream

Presented as Paper 2004-0391 at the AIAA 42nd Aerospace Sciences Meeting, Reno, NV, 5–8 January 2004; received 29 February 2004; revision received 21 April 2004; accepted for publication 20 May 2004.

*Research Scientist, Institute of Aerodynamics and Flow Technology.
†Aerodynamic Methods Engineer.
‡Research Engineer.

Introduction

FROM aircraft industry as well as from research institutes point of view, one of the most important tasks for numerical aircraft aerodynamics is the availability of a highly accurate, reliable, efficient, and validated method for solving the Reynolds-averaged Navier–Stokes equations to predict lift, drag, and moments. It is well known that computational fluid dynamics (CFD) has shown significant improvements over the last 10 years. The complexity of configurations being investigated with CFD has increased so that today complete aircraft with deployed high-lift devices can be analyzed.[1–4] Although a large effort has been conducted for verification and validation, for example in the MEGAFLOW or elsA project, the accurate prediction of drag and moments for any type of aircraft and for the complete flight envelope is still a challenge.[4]

In addition to internal CFD drag-prediction programs, Airbus and DLR, German Aerospace Center, participated in the First AIAA CFD Drag Prediction Workshop.[5,6] The DLR-F4 wing-fuselage transport aircraft model has been used, and it was found

that the drag prediction was fairly accurate and that CFD can be used for design decisions based on incremental drag only when a well-validated software system is used. Nevertheless the data of all participants varied statistically more than expected, and the need for a higher accuracy and an error estimation procedure was identified.[7] Because of the substantial interest, a second workshop had been initiated by the committee. Because the workshop was found to be very useful, DLR and Airbus decided to participate in the second workshop and were joined by ONERA. The second drag prediction workshop, DPW-2, took place in June 2003 in combination with the 21st AIAA Applied Aerodynamics Conference.[§]

For the second workshop the DLR-F6 model was selected by the committee, and DLR and ONERA have made the configuration and wind-tunnel data available. The DLR-F6 model has been used several times in the 1990s in a joint effort of ONERA and DLR to understand airframe-engine interference effects for different engine concepts and to obtain substantial data sets for CFD validation.[8–10] Compared to the DLR-F4, the DLR-F6 has increased geometric complexity and also has areas of flow separation at transonic flow conditions on the wing upper and lower side for one engine position, which makes this case challenging.

DLR, Airbus, and ONERA decided to cooperate closely for the participation in the second workshop. The work has been shared in a way that Airbus has focused its activities mainly on the computations using structured grid techniques and the far-field drag extraction method, whereas DLR has applied the unstructured, hybrid technique. ONERA has extended its far-field method to unstructured data sets so that drag-extraction results from structured and unstructured Reynolds-averaged Navier–Stokes (RANS) solvers can be compared.

The objectives of this work are to present the achieved results for the mandatory and the optional cases of the workshop and to apply two different methods for the calculation of drag. First, drag can be computed by integrating surface values of pressure and shear stress. This is called the near-field method. Another more complex technique is the integration of physical drag components, like viscous, wave, and induced drag using control volumes in the flowfield, the so-called far-field method. This physical breakdown of drag is helpful for the aerodynamic design process because, for example, areas of wave drag can be identified and an aerodynamicist can propose a redesign in those regions. Here both methods will be applied for the RANS calculations on structured and unstructured grids.

The following sections will describe the DLR-F6 model and experimental data only briefly because more details can be found in the DPW-2 summary paper.[7] This paper focuses on the workshop results from Airbus, ONERA, and DLR.

DLR-F6 Aircraft Configuration

Geometry

The DLR-F6 model with axisymmetrical through-flow nacelles, which are similar to a CFM-56 long nacelle, is used for the workshop. The configuration was designed approximately 25 years ago based on the experience with the DLR-F4 model. The objective of the DLR-F6 design was to achieve a more elliptic lift distribution and a reduced tendency towards a flow separation on the rear end of the upper side of the wing. The fuselage was not changed while three of the four defining airfoil sections of the wing had been modified. The airfoil at the kink was translated upwards to achieve a smoother wing upper surface. The twist distribution and the spanwise position of one section was moved from $\eta = 0.7$ to 0.84. The nacelle is located at $x_{\mathrm{TE}}/c = 0.49$ and $z_{\mathrm{TE}}/c = -0.189$, where x_{TE} and z_{TE} characterize the horizontal and vertical distance of the nacelle upper trailing edge to the wing leading edge, respectively, and c is the local chord length of the wing at the engine location. Details about the sizes of the geometry can be found in the literature.[7,8,10] For the workshop the configurations with [DLR-F6 wing-body-nacelle pylon (WBNP)] and without pylon/nacelle [DLR-F6 wing-body (WB)] are used.

Table 1 Grid densities (10^6 nodes)

Configuration grid level	WB	WBNP	WB	WBNP
	Structured		Unstructured	
Initial	3.0	4.6	3.8	5.5
Medium	5.5	8.5	5.8	8.2
Fine	10.0	13.7	8.8	12.3

The CAD geometry has been rebuilt completely based on the original airfoils and a wing deformation as a result of the loads. A finite element analysis of the exact wing of the model at design flow conditions resulted in an upward bending of approximately 4 mm and a twist of -0.314 deg at the wing tip. This has been included into the new CAD model. A measurement of the wind-tunnel model has been performed with a tolerance of 0.05 mm. The comparison of the CAD geometry and the wind-tunnel model shows that the wing shape is error free. The rebuilt DLR-F6 CAD model includes blunt trailing edges on all components. The curvatures of the surfaces have been checked, and initial flow calculations for the WB configuration (with/without wing deflection) have been performed before the final CAD model was released by the workshop committee.

Wind-Tunnel Tests

Several wind-tunnel test campaigns have been conducted in the 1990s in the ONERA S2MA facility. The model was rear sting mounted in the test section. The test program included a variation of the Mach number $M_\infty = 0.6 \ldots 0.85$ and the lift coefficient $C_L = 0 \ldots 0.6$. The Reynolds number was kept constant at $Re = 3 \times 10^6$. Data corrections caused by nonhomogeneous flow in the test section have been applied. The Mach number was measured at the wind-tunnel wall. The correction for the Mach number in the middle of the test section was $\Delta M = -0.002$. The influence of the wind-tunnel walls and the model support was determined as $\Delta M = -0.0005$, $\Delta\alpha = 0.023$ deg, $\Delta C_L = 5.8 \times 10^{-4}$ for the design point $M_\infty = 0.75$, $C_L = 0.5$. Additional information about the tests and the configuration can be found in previous publications.[8,9]

Grid Generation and RANS Solvers

Grid Generation

For the calculations using the structured grid technique the grids provided by the workshop have been used. The grids for both configurations have been generated by the ICEM Hexa software trying to take into account the guidelines for grid construction of the workshop committee. Three different grid levels for grid-refinement studies had been available. The effective refinement between the coarse, medium, and fine grid was approximately two, but the wing chordwise grid spacing was not refined adequately.[7]

The initial hybrid grids, consisting of prismatic, tetrahedral, and pyramidal elements, have been generated with the Centaur software from CentaurSoft.[11,¶] The wing is meshed with anisotropic triangles using a moderate stretching in spanwise direction of approximately three. The boundary layer has been captured using 25 layers of prismatic elements. The growth of the tetrahedral elements directly behind the wing was limited to avoid a quick dissipation of the velocity profile in the wake caused by a coarse grid. The initial grids have been adapted using the TAU software to obtain the coarse, medium, and fine grids. The adaptation has the advantage that less grid points are needed than for a uniform refinement to get a similar result.[12] The grid adaptation also ensures that a y^+ of approximately one is fulfilled. A detailed description of the different grids can be found in the DPW-2 summary paper.[7] The grid densities are listed in Table 1. Figure 1 shows a cut through the initial and the fine hybrid grids for the WBNP configuration. The refinement of the elements in the field is visible.

[§]Data available online at http://ad-www.larc.nasa.gov/tsab/cfdlarc/aiaa-dpw [cited June 2003].

[¶]Data available online at http://www.centaursoft.com [cited 2004].

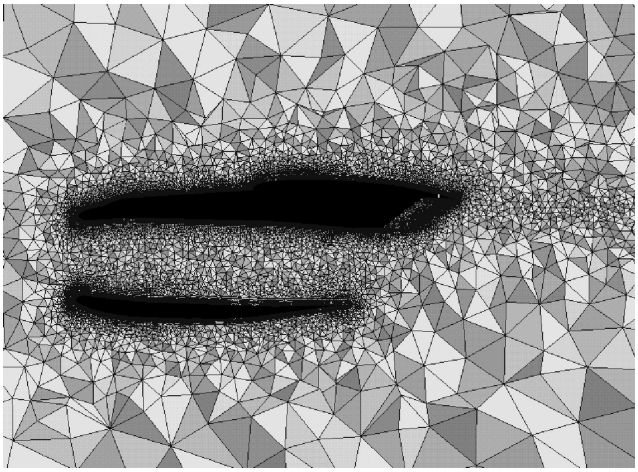

a) Initial grid

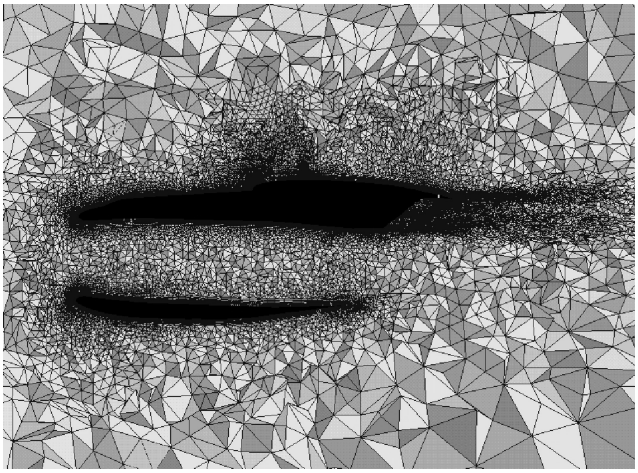

b) Fine grid

Fig. 1 Field cut through wing, pylon, and through-flow nacelle for the initial and fine grids.

Structured RANS Solver elsA

The computations on the structured grids have been carried out with the ONERA object-oriented software elsA.[13,14] The k-ω turbulence model of Wilcox was used.[15] A Jameson-type scalar dissipation and an implicit time integration scheme have been applied.

Unstrucutred RANS Solver TAU

The DLR TAU software is a finite volume vertex-based solver with an edge-based data structure. Together with a dual-grid technique, the use of different element types is possible. For these investigations a central differencing scheme and a Jameson-type scalar dissipation have been used. Time integration to steady state was accomplished with a Runge–Kutta scheme. For convergence acceleration local time stepping, residual smoothing, multigrid, and message-passing-interface (MPI)-based parallelization was applied.[16] The Spalart–Allmaras turbulence model with Edwards modifications and the k-ω-SST model have been used.[17,18]

Far-Field Drag-Extraction Method

Drag is usually extracted from numerical solutions of the RANS equations by integration of the stresses at the surface of the aircraft. In this near-field approach, total drag can be broken down into pressure drag D_p and friction drag D_f; here it is termed the mechanical breakdown. In the far-field approach, the physical components of drag, like viscous drag D_v, wave drag D_w, and induced drag D_i, are computed as integrals involving control volumes or surfaces within the flowfield. The physical breakdown of drag is considered by design engineers to be more useful than the mechanical breakdown method.

The far-field drag extraction method used here is based on a formulation from J. van der Vooren.[19] Field quantities involved in this formulation are the following:

$$\Delta\bar{u} = u_\infty \sqrt{1 + 2\frac{\Delta H}{u_\infty^2} - 2\frac{(e^{\Delta s/R})^{(\gamma-1)/\gamma} - 1}{(\gamma-1)M_\infty^2}} - u_\infty \tag{1}$$

where Δs, ΔH are entropy and stagnation enthalpy relative to their freestream value, and ∞ denotes the freestream state,

$$\boldsymbol{f}_{vw} = -\rho\Delta\bar{u}\boldsymbol{q} \tag{2}$$

and

$$\boldsymbol{f}_i = -\rho(u - u_\infty - \Delta\bar{u})\boldsymbol{q} - (p - p_\infty)\boldsymbol{i} + \boldsymbol{\tau}_x \tag{3}$$

where (x, y, z) is an orthogonal coordinate system, x being in the freestream direction, $\boldsymbol{i}$ is the unit vector in the freestream direction, and $\boldsymbol{\tau}_x$ is the vector of viscous deviatoric stresses of components τ_{xx}, τ_{xy}, τ_{xz}.

The theory is based on the assumption that production of viscous drag and wave drag is confined to finite control volumes V_V (boundary layers and viscous shear layers) and V_W (shock layers) and that the flow can be considered as inviscid outside these volumes. If V_V and V_W can be defined without overlap, viscous drag D_v and wave drag D_w can be expressed as

$$D_v = \int_{V_V} div\boldsymbol{f}_{vw}\,\mathrm{d}V \tag{4}$$

$$D_w = \int_{V_W} div\boldsymbol{f}_{vw}\,\mathrm{d}V \tag{5}$$

and induced drag D_i, in the case of a nonpropelled aircraft, as

$$D_i = \int_{V_V+V_W} div\boldsymbol{f}_i\,\mathrm{d}V - \int_{S_A} (\boldsymbol{f}_i \cdot \boldsymbol{n})\,\mathrm{d}S \tag{6}$$

where S_A denotes the closed surface of the aircraft, with the unit normal vector $\boldsymbol{n}$ pointing toward the inside of the aircraft.

This formulation requires no small disturbance assumption and ensures an exact near-field/far-field drag balance:

$$D_p + D_f = D_v + D_w + D_i \tag{7}$$

In the application to numerical solutions of the RANS equations, two significant deviations from this theory must be accounted for.[20] The first one is the possible production of spurious viscous drag outside the volumes V_V and V_W as a result of artificial dissipation or truncation errors. The second one is the spurious diffusion of tip vortices in the far-field grid, which causes a loss of induced drag through transformation into viscous drag.

This formulation can be slightly modified, shifting the viscous constraint term, $\boldsymbol{\tau}_x$ from vector $\boldsymbol{f}_i$ to vector $\boldsymbol{f}_{vw}$, which leads to different formulas for D_v and D_i (Ref. 20). This variant enables an easier implementation, hardly altering the results.

Test Cases

For each configuration two required and two optional test cases have been defined.

1) Case 1, grid-refinement study (required): $M_\infty = 0.75$, and $C_L = 0.5 \pm 0.001$, fully turbulent; usage of coarse, medium, and fine grid.

2) Case 2, drag polar (required): $M_\infty = 0.75$, and $\alpha = -3, -2, -1.5, -1, 0, 1$, and 1.5 deg; fixed transition, medium or own best practice grid.

3) Case 3, influence of transition (optional): $M_\infty = 0.75$, and $C_L = 0.5 \pm 0.001$; comparison of fully turbulent and fixed transition, medium or own best practice grid.

4) Case 4, Mach drag rise (optional): $C_L = 0.5 \pm 0.001$, and $M_\infty = 0.5, 0.6, 0.7, 0.72, 0.74, 0.75, 0.76, 0.77$; same transition setting as in case 2, medium or own best practice grid.

Results

First of all, the unstructured grid results using the standard near-field drag extraction method are presented. Following this, selected structured and unstructured results are compared using the far-field drag extraction method.

Near-Field Drag Extraction

Case 1

The influence of the grid density on the angle of incidence, drag, and pitching moment is presented for both configurations for the unstructured TAU code in Figs. 2–4. A grid refinement causes a small decrease of the overall drag. The calculated pitching moment is also slightly influenced by the grid density. The WBNP results show a larger dependency on the grid density, especially when moving from the coarse to the medium grid. This configuration shows flow separation not only on the upper wing like the WB does but also on the lower wing close to the inboard side of the pylon.[10] Only a small grid influence on the pressure is visible as presented in Fig. 5 for a section close to the inboard side of the pylon. The differences between the experimental and computed pressure distributions cause the differences of the measured and calculated pitching moment. For the WBNP configuration a strong flow acceleration is visible on the wing lower side as a result of the close coupling of the nacelle. The pressure distributions on the pylon inboard and outboard sides and on the nacelle show only small influences of the grid density.

The numerical investigations for the DLR-F6 have shown that differences in the measured and calculated pressure distributions are partly caused by a discrepancy in the wing upper- and lower-side flow separations. Figures 6 and 7 demonstrate the oil-flow pictures of the wing upper and lower sides. A trailing-edge separation on the outer part of the wing and at the wing-fuselage junction is visible. The TAU results using the Spalart–Allmaras turbulence model show smaller trailing-edge separations than observed in the experiments, whereas the separation on the wing lower side for the WBNP is predicted larger. Additional grid-resolution studies at the wing trailing edge with up to 40 elements on the base have shown that a larger separation on the upper side at the trailing edge cannot be obtained

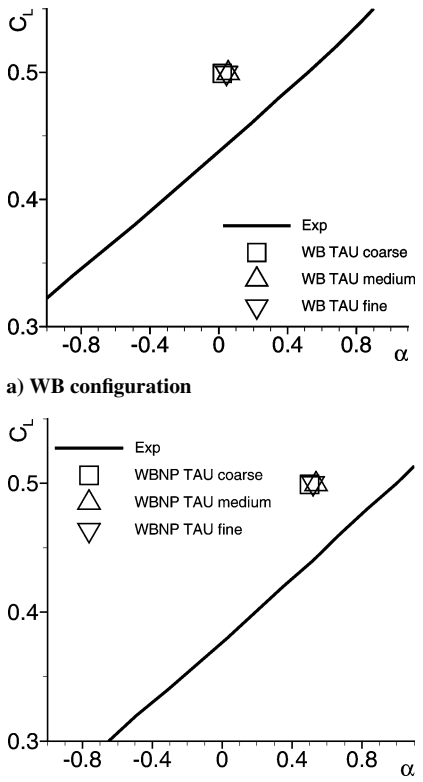

a) WB configuration

b) WBNP configuration

Fig. 2 Grid influence on angle of incidence; $M_\infty = 0.75$, and $C_L = 0.5$.

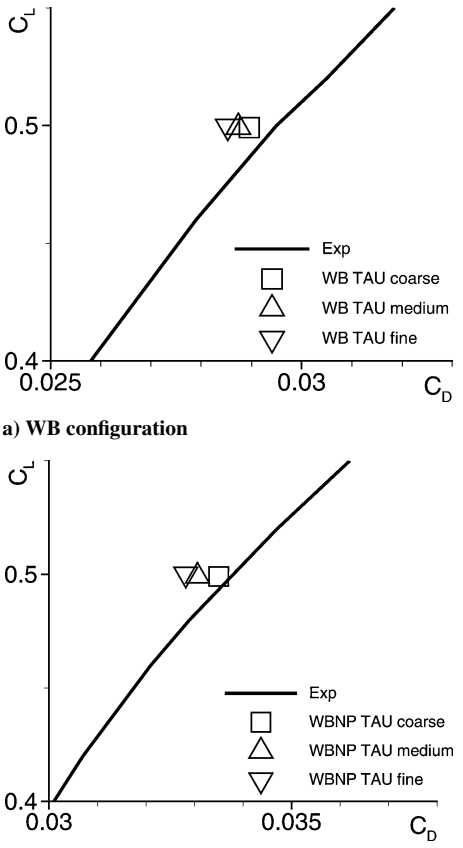

a) WB configuration

b) WBNP configuration

Fig. 3 Grid influence on drag: $M_\infty = 0.75$, and $C_L = 0.5$.

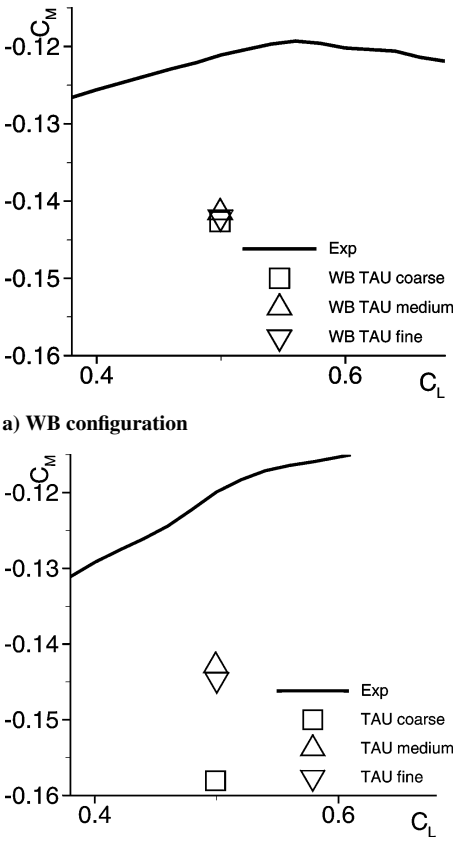

a) WB configuration

b) WBNP configuration

Fig. 4 Grid influence on momentum: $M_\infty = 0.75$, and $C_L = 0.5$.

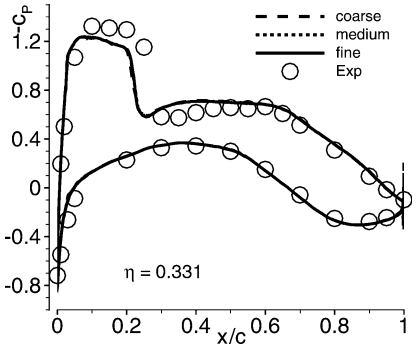

a) WB configuration

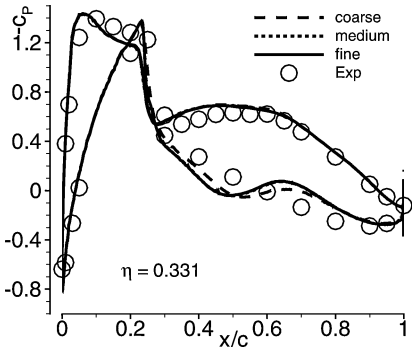

b) WBNP configuration

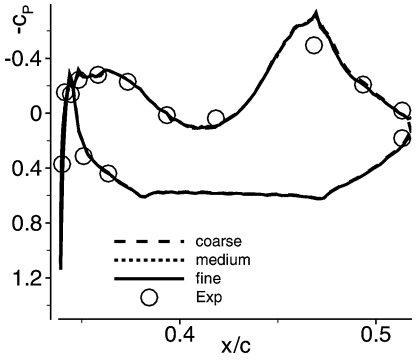

c) Nacelle, 300 deg

Fig. 5 Grid influence on pressure distributions: $M_\infty = 0.75$, and $C_L = 0.5$.

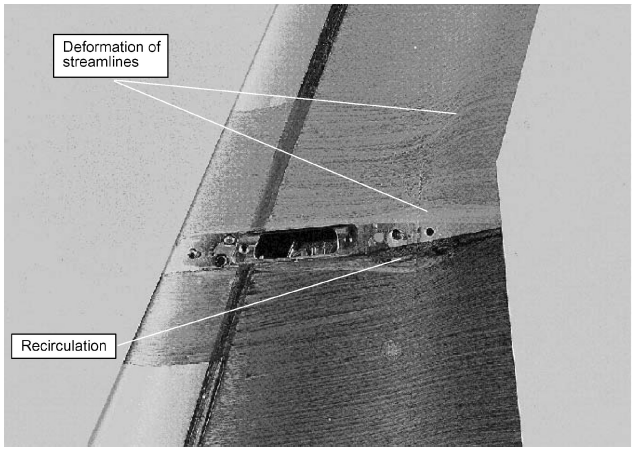

a) Experiments, demounted pylon, oil-flow visualization

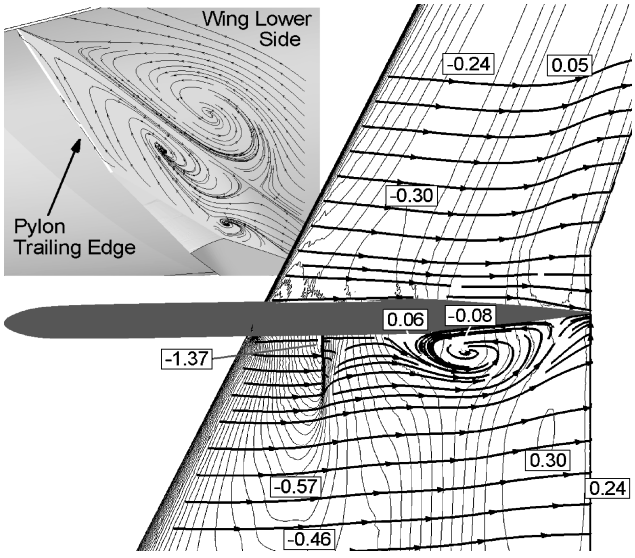

b) TAU, Spalart–Allmaras turbulence model, iso-c_P contour lines, streamlines

Fig. 7 WBNP oil-flow visualization, near-wall streamlines, wing lower and pylon inboard side: $M_\infty = 0.75$, and $C_L = 0.5$.

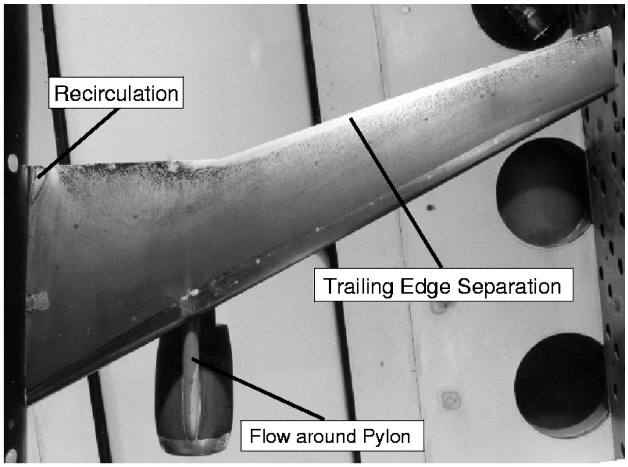

a) Experiments, oil-flow visualization

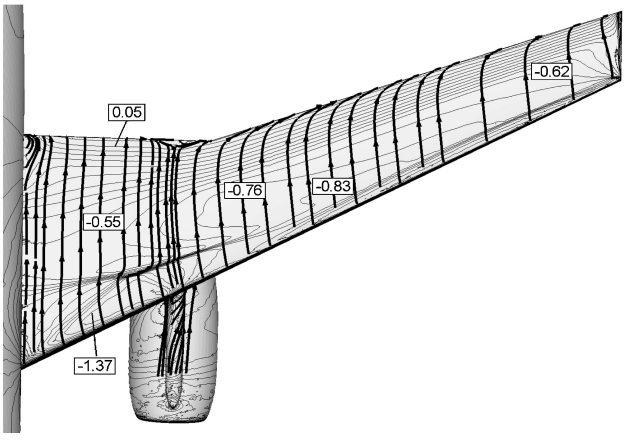

b) TAU, Spalart–Allmaras turbulence model, iso-c_P contour lines, streamlines

Fig. 6 WBNP oil-flow visualization, near-wall streamlines, wing upper side: $M_\infty = 0.75$, and $C_L = 0.5$.

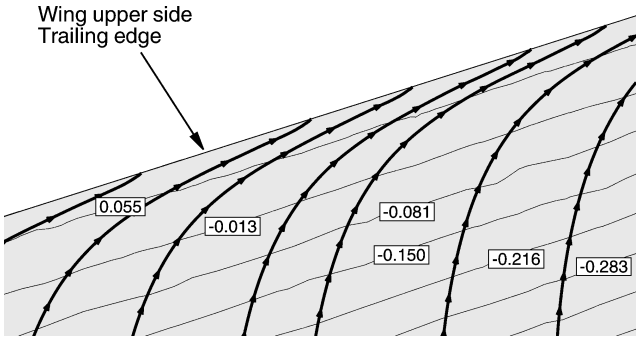

a) TAU, Spalart–Allmaras turbulence model

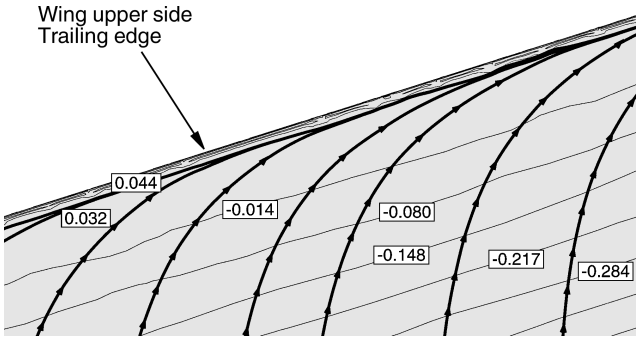

b) TAU, k-ω-SST turbulence model

Fig. 8 WB, TAU: influence of the turbulence model on the wing upper-side trailing-edge separation, iso-c_P contour lines, streamlines; $M_\infty = 0.75$, and $C_L = 0.5$.

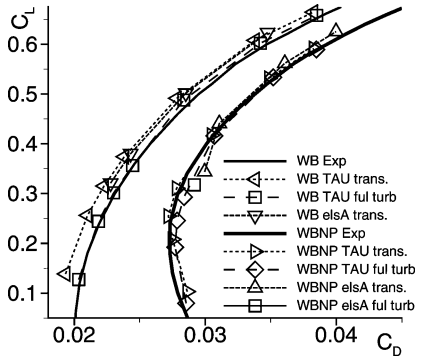

Fig. 9 TAU and elsA results, drag polars: $M_\infty = 0.75$.

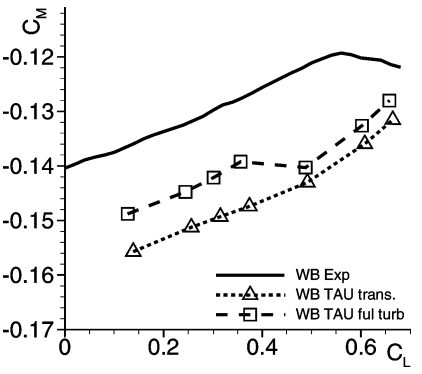

a) WB

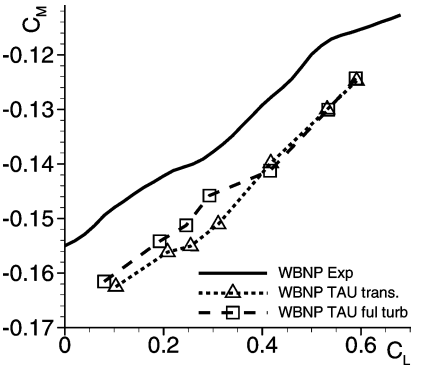

b) WBNP

Fig. 10 TAU results, moments: $M_\infty = 0.75$.

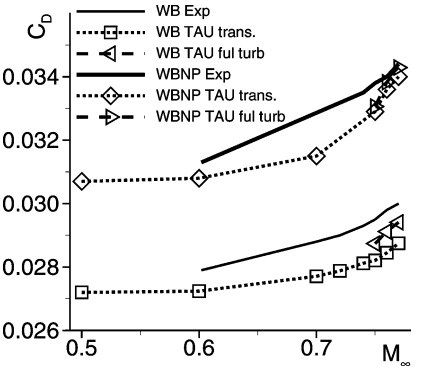

Fig. 11 TAU results, Mach drag rise: $C_L = 0.5$.

by simply increasing the number of grid points. An improvement of the wing upper-side trailing-edge separation can be achieved when the k-ω-SST turbulence model is applied. Figure 8 shows the influence of the turbulence models on the wing upper-side trailing-edge separation in an outboard section of the wing for the WB configuration.

Case 2

The comparison of the computed and the measured drag polars are plotted for both configurations in Fig. 9. In principle, slightly lower drag values can be observed for the results with the fixed transition setting. The fully turbulent calculations increase the drag slightly. The pitching moment in Fig. 10 shows a larger discrepancy as already seen in case 1.

Figure 9 compares the elsA and TAU results using the near-field integration method. All of the computations are with enforced transition, as specified during the tests. (For the elsA calculations the transition is also enforced on the nacelles.) Both solvers underestimate the overall drag for both configurations. The comparison reveals very consistent results, except for the elsA computation at -1 deg on the WBPN. This is caused by the inappropriate transition setting of 25% local chord length on the wing lower side for such an angle of incidence. It is likely that the transition occurs further upstream. This inconsistency leads to a larger flow separation on the lower side of the wing because of the laminar state of the boundary layer. However, a fully turbulent computation shows a more plausible result.

Case 3

A comparison of the fully turbulent and the fixed transition TAU results show nearly no influence of fixed transition on the pressure distributions. Only a small difference for the WBNP is visible. Nevertheless the small differences in the pressure distributions affect the pitching moment as seen in Fig. 10. The influence of fixed transition on drag can be seen in Fig. 9.

Case 4

The variation of the Mach number for $C_L = 0.5$ is plotted for both configurations in Fig. 11. The drag for the WB configuration increases slightly more slowly in the computations with increasing Mach number possibly as a result of the underpredicted development of the trailing-edge separation on the upper wing. For the WBNP configuration the differences are less pronounced. It is assumed that

this is caused by a compensation of the smaller upper-wing and the larger lower-wing separation.

Far-Field Drag Extraction

Among the numerical solutions obtained by DLR with the TAU code and Centaur hybrid grids, four were postprocessed with the drag-extraction software FFD for unstructured and hybrid grids. The drag values for the configurations, the level of grid refinement, and the aerodynamic conditions are listed in the Tables 2–4. They are expressed as drag counts. The numerical values of the drag coefficients (near-field breakdown and far-field breakdown) for the elsA results are given in the Tables 5–7.

Total drag integrated in the far field ($C_D = C_{\mathrm{Dv}} + C_{\mathrm{Dw}} + C_{\mathrm{Di}}$) is approximately seven drag counts lower than the total near-field drag ($C_D = C_{\mathrm{Dp}} + C_{\mathrm{Df}}$) with TAU and two to three drag counts with elsA. This difference comes from the elimination of spurious drag sources in the far-field integration. It has to be noted that all computed total drag values (near field and far field) are 6 to 17 drag counts below the experimental data ($C_{D-\mathrm{Experiment}} = 295$ drag counts for WB, $C_{D-\mathrm{Experiment}} = 338$ drag counts for WBPN). It has to be mentioned that a computed near-field drag level lower than the experimental level cannot be brought closer to the experiment by removing spurious drag sources.

In the far-field extraction method, the volumes V_V and V_W for the integration of viscous drag and wave drag are defined according to physical criteria.[21] The integration of D_v and D_w within these volumes allows the elimination of the spurious drag sources located outside of them. This is illustrated in Fig. 12, in a spanwise section located on the inner side of the nacelle. Two shock waves can be distinguished in this figure, one on the upper surface of the wing and the other between the lower surface of the wing, the inner side of the pylon, and the top of the nacelle.

Table 2 Near-field drag components, TAU, (10^{-4})

Configuration	Grid	C_{Dp}	C_{Df}
WB ($C_L = 0.5$)	Fine	161.0	125.3
WBNP ($C_L = 0.5$)	Fine	178.9	149.1
WBNP ($C_L = 0.5$)	Medium	179.9	149.1
WBNP ($C_L = 0.6$)	Medium	235.4	146.9

Table 3 Far-field drag components, TAU, (10^{-4})

Configuration	Grid	C_{Dv}	C_{Dw}	C_{Di}
WB ($C_L = 0.5$)	Fine	188.6	1.3	89.6
WBNP ($C_L = 0.5$)	Fine	226.3	4.8	89.6
WBNP ($C_L = 0.5$)	Medium	227.7	4.8	89.2
WBNP ($C_L = 0.6$)	Medium	235.5	14.0	125.2

Table 4 Near-/far-field drag, TAU, (10^{-4})

Configuration	Grid	C_D(near)	C_D(far)
WB ($C_L = 0.5$)	Fine	286.3	279.5
WBNP ($C_L = 0.5$)	Fine	328.0	320.7
WBNP ($C_L = 0.5$)	Medium	329.0	321.7
WBNP ($C_L = 0.6$)	Medium	382.3	374.7

Table 5 Near-field drag components, elsA, (10^{-4})

Configuration	Grid	C_{Dp}	C_{Df}
WB ($C_L = 0.5$)	Medium	149.5	135.0
WBNP ($C_L = 0.5$)	Medium	173.4	159.1

Table 6 Far-field drag components, elsA, (10^{-4})

Configuration	Grid	C_{Dv}	C_{Dw}	C_{Di}
WB ($C_L = 0.5$)	Fine	191.0	0.9	91.2
WBNP ($C_L = 0.5$)	Medium	232.3	4.8	92.5

Table 7 Near-/far-field drag, elsA, (10^{-4})

Configuration	Grid	C_D(near)	C_D(far)
WB ($C_L = 0.5$)	Medium	284.5	283.1
WBNP ($C_L = 0.5$)	Medium	332.5	329.6

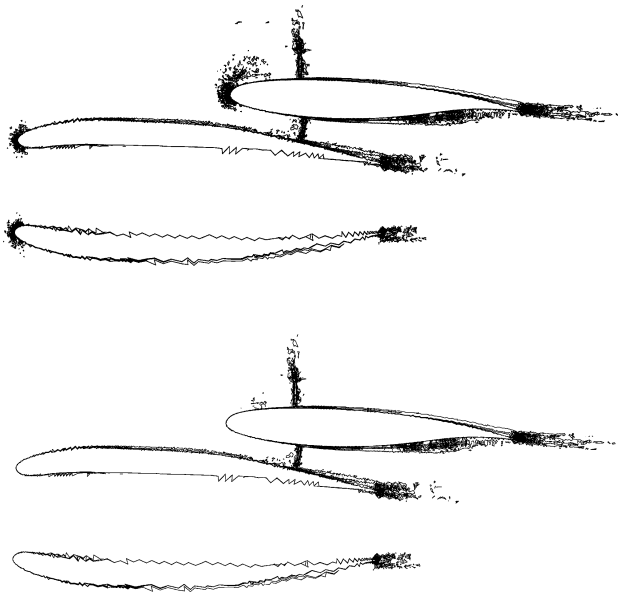

Fig. 12 WBNP: TAU, elimination of spurious drag sources in the far-field drag extraction, spanwise section on the inner side of the nacelle; $M_\infty = 0.75$, and $C_L = 0.5$.

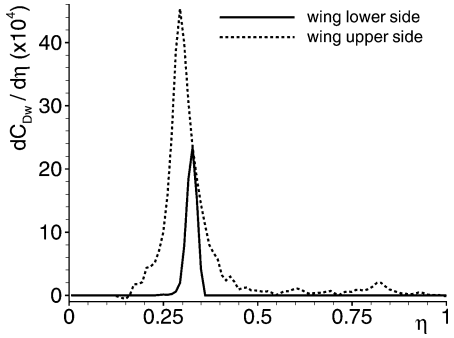

Fig. 13 WBNP: TAU, spanwise wave drag distribution; $M_\infty = 0.75$, and $C_L = 0.5$.

Installation drag, defined here as the overall drag of the WBPN configuration (including the nacelle internal drag) minus the drag of the WB configuration, is 41.7/48.0 drag counts for the near-field integration and 41.2/46.5 drag counts for the far-field integration with TAU and elsA, respectively. The experimental value is 43 drag counts.

As far as the difference between the TAU and the elsA far-field results is concerned, the largest discrepancy appears for the viscous term. One possible influence is the way of computing the viscous tensor because this component is very sensitive to its method of assessment. Furthermore, the grid density in the boundary layer is different and can have an influence on the viscous pressure drag as well. Nevertheless, a good agreement of the wave-drag magnitude and of the results for the induced drag are found. The differences of the induced drag (see Tables 3 and 6) could be caused by a different vortex shed at the wing root, which can dissipate earlier for the unstructured results as a result of the grid resolution in that area. Therefore the structured results show a higher induced drag.

Far-field drag extraction provides not only a physical breakdown of the drag, but also local distributions of wave drag and viscous drag. Figure 13 shows the spanwise distribution of wave drag for the WBPN case for $M_\infty = 0.75$, $C_L = 0.5$ computed separately on the two sides of the wing.

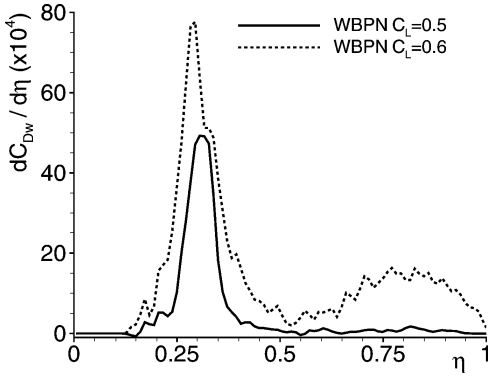

Fig. 14 WBNP: TAU, spanwise wave drag distribution; $M_\infty = 0.75$, $C_L = 0.5$, and $C_L = 0.6$.

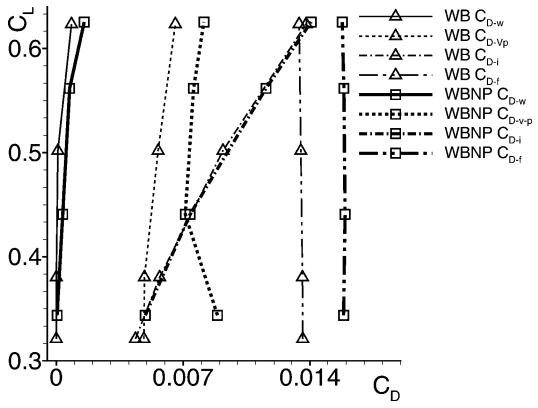

Fig. 15 WBNP: elsA; $M_\infty = 0.75$, and $C_L = 0.5$.

On the upper side, the production of wave drag is essentially located in the inner part of the wing. The wave drag on the lower side amounts to 0.8 drag counts out of an overall wave-drag coefficient of 4.8 counts. The level of wave drag of the WB configuration for the same C_L is 1.3 drag counts. The overall installation wave drag is 3.5 counts, 0.8 counts coming from the direct effect of the installation and 2.7 counts produced via the increment of angle of attack necessary to recover the required C_L.

Figure 14 shows the alteration of the spanwise wave-drag distribution for the WBPN configuration at $M_\infty = 0.75$ from $C_L = 0.5$ to $C_L = 0.6$. The critical areas of the wing appear as the maxima of the distribution at the higher C_L. Such data illustrated in Figs. 13 and 14 are of great interest for aircraft designers.

A full postprocessing of the elsA computations enables the drag breakdown shown in Fig. 15. It can bring some interesting elements for discussion. For example, concerning the wave drag, the contribution of the lower side of the wing caused by the engine installation is clearly visible at low C_L. As far as the induced drag is concerned, one can conclude that the engine installation has quite a low impact on this component. The unexpected drag increase observed on the polar for $\alpha = -1.0$ deg for the WBNP configuration comes from an increase of viscous pressure drag. It confirms that this increase is caused by a large flow separation, as discussed earlier. It probably means that the location of the enforced transition is not adequate on the lower side of the wing.

The comparison of the wave and the viscous drag for the structured (elsA) and unstructured (TAU) results shows a good agreement of the magnitude and of the local drag rise in spanwise distribution as visualized in Fig. 16. The viscous drag caused by the fuselage is identically predicted, as well as the local rise, which means in particular that the root flow separation is very similar for both codes. It shows that both solvers have identified the same flow features at the same place. Furthermore, the presence of the nacelle affects the distribution in the same way for both solvers, with a particularly good agreement on the position. The identified volume V_W is plotted in

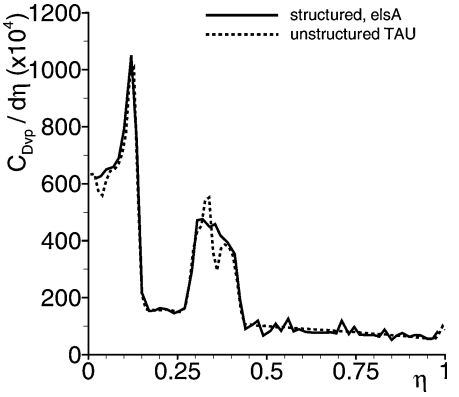

a) Viscous drag

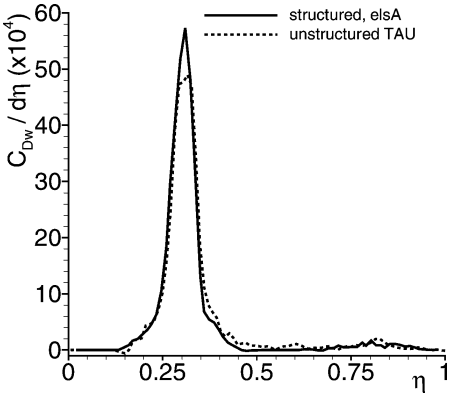

b) Wave drag

Fig. 16 WBNP: spanwise distribution of viscous and wave drag; $M_\infty = 0.75$, and $C_L = 0.5$.

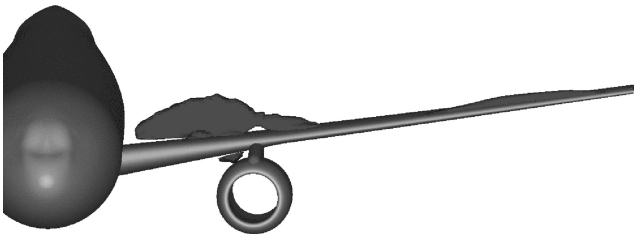

Fig. 17 WBNP: elsA, medium grid, wave-drag volume V_w; $M_\infty = 0.75$, and $C_L = 0.5$.

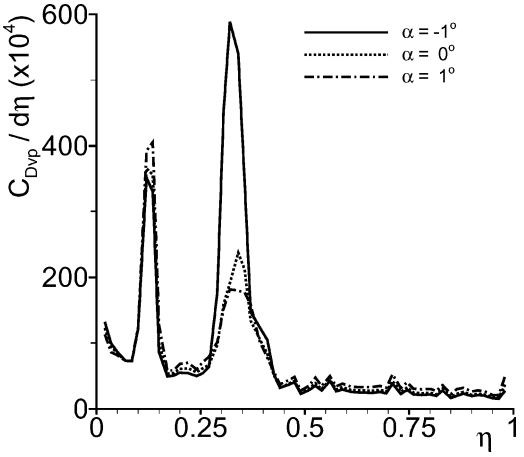

Fig. 18 WBNP: elsA, spanwise distribution of viscous pressure drag, variation of angles of incidence; $M_\infty = 0.75$.

Fig. 17 and gives an impression about the areas, that contribute to the wave drag.

Plotting the spanwise distribution of viscous pressure drag for several angles of incidence, as shown in Fig. 18, clearly highlights the presence of the massive separation on the inboard side of the pylon. Therefore, this example of correlation confirms that the far-field drag method can provide very usable information. It enables the aerodynamic designer to identify specific flow features and make the analysis of a numerical solution more reliable.

Conclusions

It can be concluded that the numerical evaluation and breakdown of the overall drag from Reynolds-averaged Navier–Stokes computations about the WBNP configutation provides accurate information compared to experimental data. The strong flow separations for this configuration on both sides of the wing cause a slightly higher offset of experimental and numerical results than known from other aircraft configurations. As far as the actual overall drag accuracy is concerned, it is necessary to further investigate similar configurations and cases that show also trailing-edge flow separations.

The engine installation drag, which in principle is the difference of the drag of two configurations (with/without engine and pylon), can be computed with an accuracy of approximately 1% showing that decisions on the aerodynamic design can be made based on well-validated Reynolds-averaged Navier–Stokes solvers. A detailed analysis of the flow features reveals that in principle all areas of flow separations on the DLR-F6 can be identified but that the sizes of those areas are slightly under (upper wing) or overpredicted (lower wing) resulting in systematic deviations of the pressure distributions and pitching moments. A variation of the grid resolution is not sufficient to correctly predict the flow separation on the upper-wing trailing edge, whereas the application of the k-ω-SST turbulence model produces a better prediction of the flow separation.

The far-field method shows that similar physical drag components can be computed from the structured and unstructured solver results despite the fact that different grids, different turbulence models, and different solvers have been used. This indicates that both solvers are capable of capturing the flow physics to a similar level of accuracy, and, more importantly, it shows that the far-field method is a useful technique to achieve very valuable information for aerodynamic design.

The Second AIAA CFD Drag Prediction Workshop again has been found to be useful to identify deficiencies of drag methods and to trigger further developments of high-accuracy drag-prediction techniques for aircraft aerodynamics.

Acknowledgments

The authors wish to thank their respective companies and research organizations for their support. Special thanks go to Arno Ronzheimer and Lars Lekemark, for doing the CAD preparation and to Stefan Melber, all DLR, for performing the TAU computations using the k-ω-SST turbulence model.

References

[1]Mavriplis, D. J., and Pirzadeh, S., "Large-Scale Parallel Unstructured Mesh Computations for 3D High-Lift Analysis," *Journal of Aircraft*, Vol. 36, No. 6, 1999, pp. 987–998.

[2]Kroll, N., Rossow, C.-C., Becker, K., and Thiele, F., "The MEGAFLOW Project," *Aerospace Science and Technology*, Vol. 4, No. 4, 2000, pp. 223–237.

[3]Rogers, S., Roth, K., Nash, S., Baker, M., Slotnick, J., Whitlock, M., and Cao, H., "Advances in Overset CFD Processes Applied to Subsonic High-Lift Aircraft," AIAA Paper 2000-4216, Aug. 2000.

[4]Kroll, N., Rossow, C.-C., Schwamborn, D., Becker, K., and Heller, G., "MEGAFLOW—A Numerical Flow Simulation Tool for Transport Aircraft Design," International Council of the Aeronautical Sciences, Sept. 2002.

[5]Rakowitz, M., Eisfeld, B., Schwamborn, D., and Sutcliffe, M., "Structured and Unstructured Computations on the DLR-F4 Wing-Body Configuration," *Journal of Aircraft*, Vol. 40, No. 2, 2003, pp. 256–264.

[6]Levy, D., Zickuhr, T., Vassberg, J., Agrawal, S., Wahls, R., Pirzadeh, S., and Hemsch, M., "Data Summary from the First AIAA Computational Fluid Dynamics Drag Prediction Workshop," *Journal of Aircraft*, Vol. 40, No. 5, 2003, pp. 875–882.

[7]Laflin, K., Vassberg, J., Wahls, R., Morrison, J., Brodersen, O., Rakowitz, M., Tinoco, E., and Godard, J.-L., "Summary of Data from the Second AIAA CFD Drag Prediction Workshop," AIAA Paper 2004-0556, Jan. 2004.

[8]Rossow, C.-C., Godard, J. L., Hoheisel, H., and Schmitt, V., "Investigation of Propulsion Integration Interference on a Transport Aircraft Configuration," AIAA Paper 92-3097, July 1992.

[9]Godard, J.-L., Brodersen, O., and Hepperle, M., "Aerodynamic Interference Effects with Engines of Different Bypass Ratio on the Generic F6 Transport Aircraft Configuration," *Proceedings of the 7th European Propulsion Forum: Aspects on Engine/Airframe Integration*, CEAS Confederation of European Aerospace Societies, Paris, France, 1999, pp. 75–84.

[10]Brodersen, O., "Drag Prediction of Engine-Airframe Interference Effects Using Unstructured Navier–Stokes Calculations," *Journal of Aircraft*, Vol. 39, No. 6, 2002, pp. 927–935.

[11]Kallinderis, Y., "Hybrid Grids and Their Applications," *Handbook of Grid Generation*, edited by J. F. Thompson, B. K. Soni, and N. Weatherill, CRC Press, Boca Raton, FL, 1999, pp. 25.1–25.18.

[12]Brodersen, O., "Numerische Analyse der Aerodynamischen Triebwerksinstallationseffekte an Transportflugzeugen," DLR Technical Rept., 2003-10, Cologne, April 2003.

[13]Cambier, L., and Gazaix, M., "elsA: An Efficient Object-Oriented Solution to CFD Complexity," AIAA Paper 2002-0108, Jan. 2002.

[14]Gazaix, M., Jolles, A., and Lazareff, M., "The elsA Object-Oriented Computational Tool for Industrial Applications," International Council of the Aeronautical Sciences, Toronto, Sept. 2002.

[15]Wilcox, D., *Turbulence Modeling for CFD*, DCW Industries, La Canada, CA, 1994.

[16]Gerhold, T., and Evans, J., "Efficient Computation of 3D-Flows for Complex Configurations with the DLR-Tau Code Using Automatic Adaptation," *Notes on Numerical Fluid Mechanics*, edited by W. Nitsche, H.-J. Heinemann, and R. Hilbig, Vol. 72, Vieweg, Braunschweig, 1998, pp. 178–185.

[17]Spalart, P. R., and Allmaras, S. R., "A One-Equation Turbulence Model for Aerodynamic-Flows," AIAA Paper 92-0439, Jan. 1992.

[18]Menter, F. R., "Zonal Two Equation k-ω Turbulence Models for Aerodynamic Flows," AIAA Paper 93-2906, July 1993.

[19]Van der Vooren, J., and Destarac, D., "Drag/Thrust Analysis of Jet-propelled Transonic Transport Aircraft, Definition of Physical Drag Components," *Aerospace Science and Technology*, Vol. 8, No. 6, 2004, pp. 545–556.

[20]Destarac, D., "Far-Field/Near-Field Drag Balance and Applications of Drag Extraction in CFD," *VKI Lecture Series 2003-02, CFD-Based Aircraft Drag Prediction and Reduction*, edited by H. Deconninck, K. Semeus, and C. van Dam, von Kármán Inst. for Fluid Dynamics, Brussels, Feb. 2003, Chap. 3.

[21]Tognaccini, R., "Methods for Drag Decomposition, Thrust-Drag Bookkeeping from CFD Calculations," *VKI Lecture Series 2003–02, CFD-Based Aircraft Drag Prediction and Reduction*, edited by H. Deconninck, K. Semeus, and C. van Dam, von Kármán Inst. for Fluid Dynamics, Brussels, Feb. 2003, Chap. 4.